

# A TIME WARPING MODEL FOR SEASONAL DATA WITH APPLICATION TO AGE ESTIMATION FROM NARWHAL TUSKS

BY LARS REITER NIELSEN <sup>1,a</sup>, MADS PETER HEIDE-JØRGENSEN <sup>2,d</sup>, EVA GARDE <sup>2,c</sup>, ADELINE SAMSON <sup>3,e</sup>, SUSANNE DITLEVSEN <sup>1,b</sup>

<sup>1</sup>*Department of Mathematical Sciences, University of Copenhagen, Copenhagen, Denmark*, <sup>a</sup>[lrn@math.ku.dk](mailto:lrn@math.ku.dk);  
<sup>b</sup>[suzanne@math.ku.dk](mailto:suzanne@math.ku.dk)

<sup>2</sup>*Greenland Institute of Natural Resources*, <sup>c</sup>[evga@mail.ghsdk.dk](mailto:evga@mail.ghsdk.dk); <sup>d</sup>[mhj@mail.ghsdk.dk](mailto:mhj@mail.ghsdk.dk)

<sup>3</sup> *Jean Kuntzmann Laboratory, Université Grenoble Alpes*, <sup>e</sup>[adeline.leclercq-samson@univ-grenoble-alpes.fr](mailto:adeline.leclercq-samson@univ-grenoble-alpes.fr)

Signals with varying periodicity frequently appear in real-world phenomena, necessitating the development of efficient modelling techniques to map the measured nonlinear timeline to linear time. Here we propose a regression model that allows for a representation of periodic and dynamic patterns observed in time series data. The model incorporates a hidden strictly positive stochastic process that represents the instantaneous frequency, allowing the model to adapt and accurately capture varying time scales. A case study focusing on age estimation of narwhal tusks is presented, where cyclic element signals associated with annual growth layer groups are analyzed. We apply the methodology to data from one such tusk collected in West Greenland and use the fitted model to estimate the age of the narwhal. The proposed method is validated using simulated signals with known cycle counts and practical considerations and modelling challenges are discussed in detail. This research contributes to the field of time series analysis, providing a tool and valuable insights for understanding and modeling complex cyclic patterns in diverse domains.

**1. Introduction.** Time series data with cyclic patterns are commonly encountered in real-world applications, ranging from environmental, ecological, physical and physiological studies to economic forecasting (Glass and Mackey, 1988; Shumway and Stoffer, 2017). Understanding and accurately modelling such patterns are crucial for gaining insights into underlying dynamics and making reliable conclusions.

In some applications, the measurements are taken along a segment, where each measured point at some distance corresponds to an unknown time. Key examples are tree rings, sea sediment cores, ice cores, hair, ear stones (Monserud and Marshall, 2001; Jouzel and Masson-Delmotte, 2010; Charles et al., 1996; Hüsy et al., 2021a; Mosbacher et al., 2016), or in this case, narwhal tusks. A given variable is measured along a transect line at equidistant spatial points, and the oscillation patterns in the data are hypothesized to reflect yearly variations. The measurements can then be dated, i.e., distances can be transformed to a time line.

A significant challenge presented by such datasets relates to the unknown nonlinear relation between distance and the underlying timeline, complicating the precise mapping of the signals to their actual temporal positions. In cases where reference signals are available or when the primary objective of the study centers on signal alignment rather than precise temporal mapping, methodologies like Graphical and Dynamic Time Warping (Jeong, Jeong and Omitaomu, 2011; Salvador and Chan, 2007; Wang et al., 2016) offer effective solutions for tasks involving pattern matching and classification. However, when reference signals are

---

*Keywords and phrases:* sclerochronology, stable isotope analysis, stochastic growth-time process, warping of signals from distance to time, age estimation, detecting seasonality, narwhal tusk.

absent, and the exact mapping from spatial position to real time is of particular concern, it appears that no universal method for time warping exists, to the best of our knowledge.

This paper presents a novel approach for modelling noisy non-stationary cyclic signals with changing periodicity and amplitude. As opposed to the traditional seasonal decomposition (Dagum, 2013; Cleveland et al., 1990) where a signal is split into trend, seasonal, cyclic, and noise components, our model incorporates the seasonal and cyclic effects, and combine them into a single component. A key innovation in our model is the incorporation of a hidden strictly positive stochastic process that models the (instantaneous) growth process of the material. The integral of this process is strictly increasing and models the time-growth process, which enables the modulation of frequencies while respecting the direction of time. This provides realism in capturing the varying periodicity observed in real-world data. Section 2 outlines the model, while Section 3 explains the estimation process. In section 4, we simulate from our model.

The flexibility of our model allows for a wide range of applications. For example, in ecological studies, time series data are often associated with annual cycles, such as the growth patterns of organisms where various exogenous and endogenous factors can influence the speed of growth (Stounberg et al., 2022; Amais et al., 2021; Wooller et al., 2021). Our method can effectively capture the changing frequencies and provide more accurate predictions for these cyclic patterns.

Narwhals (*Monodon monoceros*), a toothed whale endemic to the Arctic regions, exhibit annual depositions of growth layer groups (GLGs) in their tusks (Garde et al., 2024) resulting in annual cyclic patterns. We present a case study in section 5 where we demonstrate and validate our model on element signals (specifically the isotope Barium-137) derived from one narwhal tusk, and use the method to estimate the number of cycles, thereby also the age of the narwhal. We conclude with a discussion of the model in Section 6.

**2. Time warping model.** Consider a time series with an additive decomposition,

$$(1) \quad y_i = f(x_i, \theta) + \epsilon_i, \quad i = 0, 1, \dots, n; x_i = i\Delta$$

where  $y_i$  is the measured variable (e.g., a chemical element) at spatial location  $x_i$  and  $\Delta = x_{i+1} - x_i$  is the distance between measurements. The observation interval is thus  $[0, n\Delta]$ . The function  $f$  is detailed below and depends on parameters  $\theta$ . The error terms  $\epsilon_i$  are assumed independent and normally distributed with mean 0 and variance  $\sigma^2$ . The variable  $x$  is the distance along a cross section of some object of interest, where a specific position corresponds to an unknown time through a monotonic and possibly non-linear function  $g$ ,

$$(2) \quad t_i = g(x_i, \theta).$$

We impose that  $g(\cdot)$  is a strictly increasing function with respect to  $x$ , to ensure that time is not going backwards.

For the signal, we assume the form

$$(3) \quad f(x, \theta) = A \sin(g(x, \theta) + b) + \sum_{m=1}^M B_m \cos((m+1)(g(x, \theta) + b) + \pi), \quad g(0, \theta) = 0,$$

where  $(B_m)_{m=1,\dots,M}$  and  $A$  determine the amplitudes and  $b$  is the phase at  $x = 0$ . There is no trend in equation (3), and we assume it is removed in a prepossessing step, if necessary. For the signals used in our case study, no apparent trend was detected, and this paper will not address detrending techniques, of which there exists several choices [insert references]. Model (3) is composed of a sequence of  $M + 1$  trigonometric functions and measurement noise. The sine term, is the base component corresponding to a slow wave. Each added cosine function with index  $m$ , of which there are  $M$  in total, has a frequency of  $m + 1$  times

that of the sine function. In the case where  $M = 1$ , the sine wave can represent an annual cycle, while the fast cosine wave captures the summer-winter variations. See Figure 1 for a illustration.

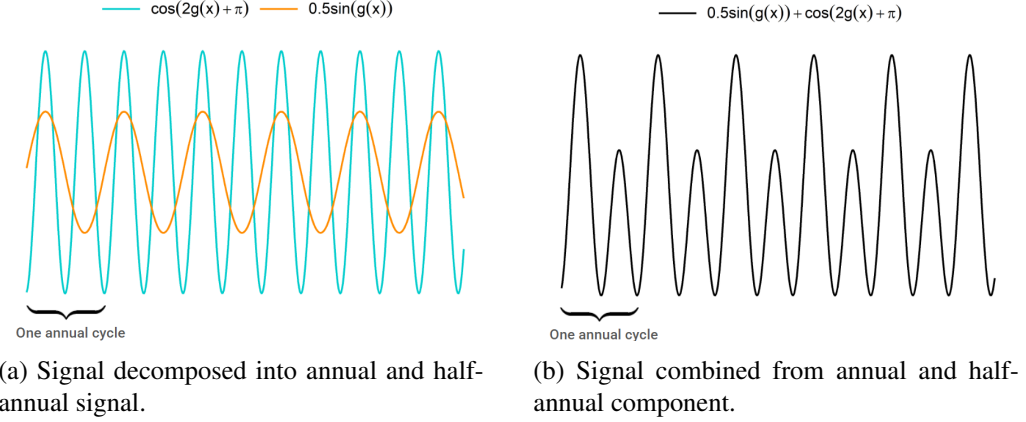


**Fig 1: Base case illustration of  $f(x, \theta)$ .** Visualization of a signal (Fig. (b)) and its decomposition into two ( $M = 1$ ) components (Fig. (a)) with constant amplitudes  $A = 0.5$  and  $B_1(x) = 1$  and no phase offset  $b = 0$ . The frequency is fixed to  $a = 0.7$ , thus  $g(x) = 0.7x$ .

In the linear and deterministic case where  $g(x, \theta) = ax$  the cycles are regularly occurring and the decomposition is known as a *seasonal* decomposition (Cleveland et al., 1990). However, this is unrealistic in most settings, where the length of one cycle will typically vary due to environmental factors. We therefore allow the instantaneous growth rate to be stochastic. We denote the unknown stochastic transformation  $g(x, \theta)$  by *the growth-time process*.

Let  $g(x, \theta) = \int_0^x \xi_s ds$  where  $(\xi_x)_{x \geq 0}$  is a positive stochastic process described by unknown parameters  $\theta$ , and which we denote by *the growth process*. For  $(\xi_x)_{x \geq 0}$ , we propose the square root diffusion process, also known as the Cox-Ingersoll-Ross (CIR) process, satisfying the stochastic differential equation (SDE)

$$(4) \quad d\xi_x = -\beta(\xi_x - a)dx + \omega\sqrt{\xi_x}dW_x, \quad \xi_0 = 0,$$

where  $W_x$  is a standard Wiener process. The hidden process  $(\xi_x)_{x \geq 0}$  describes instantaneous frequency deviations from the baseline frequency  $a/2\pi$ . The parameter  $\beta$  determines the rate of adjustment to the baseline and  $\omega$  scales the noise level. This is an ergodic process with stationary distribution the Gamma distribution with shape parameter  $2\beta a/\omega^2$ , scale parameter  $\omega^2/(2\beta)$ , mean  $a$  and variance  $a\omega^2/2\beta$ , provided that  $\beta, a, \omega > 0$ , and  $2\beta a \geq \omega^2$  (Ditlevsen, Rubio and Lansky, 2020). These parameter restrictions ensure that any solution to Eq. (4) is strictly positive (except at  $x = 0$ ) with long-term mean  $a$ , leading to a strictly increasing process  $g(x, \theta)$ . Define also the one-lag autocorrelation of the growth process  $\rho = \exp(-\Delta\beta)$  and the stationary variance  $\gamma^2 = \omega^2/2\beta$ , which will be the parameter that we estimate. The exact transition density, i.e., the distribution of  $\xi_{x+\Delta}$  given  $\xi_x$  follows a non-central  $\chi^2$  distribution scaled by a constant factor. Specifically,  $\xi_{x+\Delta} | \xi_x \sim Z_x/2c$ , where  $Z_x \sim \chi_\nu^2(\lambda_x)$  is non-central chi-squared distributed with  $\nu = \frac{4a\beta}{\omega^2}$  degrees of freedom and non-centrality parameter  $\lambda_{x+\Delta} = 2c\rho\xi_x$ . The multiplicative constant is  $\frac{1}{2c}$ , where  $c = \frac{2\beta}{(1-\rho)\omega^2}$  (Ditlevsen and Lansky, 2006).

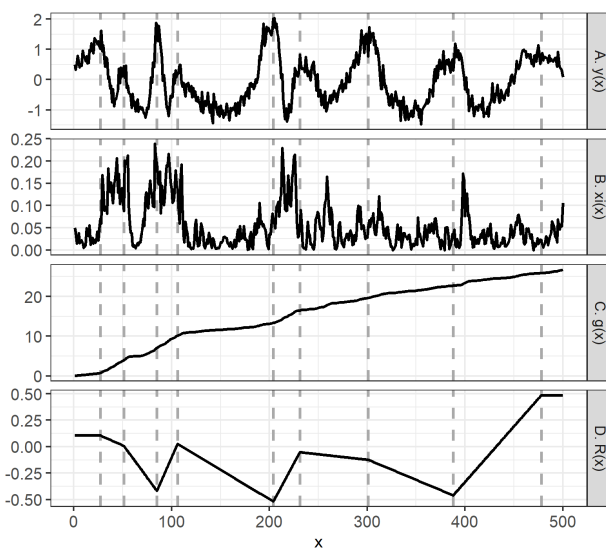


**Fig 2: Example of a simulated signal.** The dataset was simulated using  $n = 500$ ,  $\Delta = 1$ ,  $\rho = 0.82$ ,  $\beta = 0.2$ ,  $\sigma = 0.2$ ,  $A = 0.5$ ,  $B_0 = 0.8$ ,  $a = 0.05$ ,  $b = \frac{\pi}{2}$ ,  $\omega^2 = 0.01$ . The amplitude displacement parameters  $r_k$  were simulated from a zero-mean normal distribution with variance 0.25. A. Simulated signal with measurement noise  $y(x)$ . B. Simulated hidden process  $(\xi_x)_{x \geq 0}$ . C. Simulated growth-time process  $g(x)$ . D. Amplitude correction (relative to  $B_0$ ) function  $R(x)$ . Gray dashed lines are signal peaks.

TABLE 1  
Model parameters. Name, support and interpretation.

Parameter	Support	Interpretation
$A$	$(0, \infty)$	Amplitude for the base wave.
$B_m$	$(0, \infty)$	Amplitude for wave $m$ .
$b$	$(0, 2\pi)$	Phase-offset of the signal.
$\sigma^2$	$(0, \infty)$	Variance of measurements
$a$	$(0, \infty)$	Mean of instantaneous growth process
$\beta$	$(0, \infty)$	Adjustment rate of instantaneous growth process
$\rho$	$(0, 1)$	One-lag autocorrelation of instantaneous growth process, $\rho = \exp(-\Delta\beta)$
$\omega^2$	$(0, 2a\beta)$	Infinitesimal variance of instantaneous growth process
$\gamma^2$	$(0, a^2)$	Stationary variance of instantaneous growth process, $\gamma^2 = a\omega^2/2\beta$

Our main goal is to infer  $g(x, \theta)$  in order to date the observations  $y_i$  to  $t_i = g(x_i, \theta)$ ,  $i = 0, \dots, n$ . From  $g(x, \theta)$  we are also able to predict the number of cycles in the signal:

$$(5) \quad \text{Number of Cycles} = \frac{g(x_n, \theta)}{2\pi}.$$

The parameters of the model are summarized in Table 1. In Figure 2 we illustrate a signal simulated from the model (1) and (3), along with the embedded growth process(4).

### 3. Estimation.

**3.1. Preprocessing: Varying Amplitudes.** Our model requires trend-free signals with constant amplitudes. We assume that the signal has no trend component, but that the amplitudes are potentially non-constant, but slowly varying. To estimate the amplitude process

$z_i = z(x_i)$ , we apply local polynomial regression (LOESS) to the absolute value of the signal using R's `loess` function with a span of 20% of neighboring points. The signal is then transformed to have constant amplitudes by normalizing as  $y_i \leftarrow \frac{y_i}{z_i}$

**3.2. Principle of the SAEM algorithm.** Denote the unknown parameters by  $\theta := (A, B_0, a, b, \sigma^2, \beta, \omega^2)$ . Here we propose an algorithm for estimating  $\theta$  from observations  $y = (y_0, y_1, \dots, y_n)$ .

The likelihood of the data  $y_i$  is not explicit as model (3) depends on the hidden stochastic process  $(\xi_x)_{x \geq 0}$ . A common approach for finding estimators in models with latent and unobserved data is the *expectation-maximization* (EM) algorithm (Dempster, Laird and Rubin, 1977). In this iterative procedure at iteration  $m$ , the E-step is carried out by evaluating the expected log-likelihood given data and current estimates  $\hat{\theta}^{m-1}$ :

$$(6) \quad \begin{aligned} Q_m(\theta) &\stackrel{\text{def}}{=} Q(\theta | \hat{\theta}^{m-1}) \\ &\stackrel{\text{def}}{=} \mathbb{E}_{\xi | y, \hat{\theta}^{m-1}} [\ell(y, \xi; \theta) | (y; \hat{\theta}^{m-1})] \end{aligned}$$

where  $\ell$  is the complete log-likelihood of  $y$  and the hidden process  $\xi := \xi_{0:n} = (\xi_0, \dots, \xi_n)$ . The expectation is taken wrt. the probability distribution  $p(\xi | y, \hat{\theta}^{m-1})$ . In the M-step,  $Q_m(\theta)$  is then maximized in order to obtain new estimates  $\hat{\theta}^m$ :

$$(7) \quad \hat{\theta}^m = \arg \max_{\theta} Q(\theta | \hat{\theta}^{m-1}).$$

The complete log-likelihood is explicit and given by

$$\begin{aligned} \ell(y, \xi; \theta) &= \sum_{i=0}^n \log p(y_i | \xi_i) + \sum_{i=1}^n \log p(\xi_i | \xi_{i-1}) + \log p(\xi_0) \\ &= -\frac{1}{2\sigma^2} \sum_{i=0}^n (y_i - f(x_i, \theta))^2 - \frac{n+1}{2} \log \sigma^2 + \sum_{i=1}^n \log p(\xi_i | \xi_{i-1}, \theta) + \log p(\xi_0). \end{aligned}$$

As explained in Section 2, the transition density  $p(\xi_i | \xi_{i-1}, \theta)$  is a non-central  $\chi^2$ -distribution.

However, the conditional distribution of  $\xi$  given  $y$  is not explicit due to the non-linear nature of the regression function and the non-central  $\chi^2$  distribution of the transition density. Thus, we are unable to perform the E-step in eq. (6). Instead we use (a variant of) the *Stochastic Approximation EM* (SAEM) algorithm (Delyon, Lavielle and Moulines, 1999; Jank, 2006). In this procedure, the E-step is replaced by two steps, a simulation (S) step and a stochastic approximation (SA) step. In the simulation step, we use a Sequential Monte Carlo (SMC) (Del Moral, Doucet and Jasra, 2006a) sampler to draw the non-observed data  $\xi^m$ , conditionally on  $\hat{\theta}^{m-1}$ . We then apply a stochastic approximation to equation (6):

$$(8) \quad \tilde{Q}_m(\theta) = \tilde{Q}_{m-1}(\theta) + \alpha_m (\ell(y, \xi^m; \hat{\theta}^{m-1}) - \tilde{Q}_{m-1}(\theta))$$

where  $\alpha_m$  is a decreasing sequence of positive numbers quantifying the memory in the approximation process, fulfilling  $\sum_m \alpha_m = \infty$  and  $\sum_m \alpha_m^2 < \infty$ .

This algorithm can be simplified when the complete likelihood belongs to the curved exponential family, which then reduces to approximating the minimal sufficient statistics of the model during the E step, while the M step is explicit through the sufficient statistics. Nevertheless, the distribution  $p(\xi_i | \xi_{i-1})$  does not belong to a curved exponential family and we have therefore no sufficient statistics. In that case, each iteration of the EM algorithm solves

$$\partial_{\theta} \tilde{Q}_m(\theta) = 0.$$

However, solving the score function for the CIR process can be numerically unstable (Sørensen, 2012). We instead use martingale estimating functions (Bibby and Sørensen, 1995), leading to an approximated version of the EM algorithm.

**3.3. Martingale estimating function and SAEM.** At iteration  $m$  of the algorithm, given the current value  $\xi^{m-1}$  of the hidden process  $\xi$ , the M step is updated by solving the score function, i.e., by differentiating the complete log-likelihood  $\ell(y, \xi^m, \theta)$  with respect to  $\theta$ , the score function being approximated during the SA step.

Since the parameters  $a, \beta$  and  $\omega$  of the hidden process  $\xi$  are difficult to estimate from the likelihood, we use a martingale estimating score function (Sørensen, 2012). The estimator is defined directly as the solution to equating the martingale estimation function to 0, mimicking the score equation. This leads to the statistics  $S_1, S_2, S_3$  (Sørensen, 2012, p. 21):

$$(9) \quad S_1 = \frac{\frac{1}{n} \sum_{i=1}^n \xi_{i\Delta}^m / \xi_{(i-1)\Delta}^m - (\frac{1}{n} \sum_{i=1}^n \xi_{i\Delta}^m) (\frac{1}{n} \sum_{i=1}^n (\xi_{(i-1)\Delta}^m)^{-1})}{1 - (\frac{1}{n} \sum_{i=1}^n \xi_{(i-1)\Delta}^m) (\frac{1}{n} \sum_{i=1}^n (\xi_{(i-1)\Delta}^m)^{-1})};$$

$$(10) \quad S_2 = \frac{1}{n} \sum_{i=1}^n \xi_i^m + \frac{S_1}{n(1-S_1)} (\xi_{n\Delta}^m - \xi_0^m);$$

$$(11) \quad S_3 = \frac{\sum_{i=1}^n (\xi_{i-1}^m)^{-1} (\xi_{i\Delta}^m - \xi_{(i-1)\Delta}^m) S_1 - S_2(1-S_1))^2}{\sum_{i=1}^n (\xi_{(i-1)\Delta}^m)^{-1} ((\frac{1}{2} S_2 - \xi_{(i-1)\Delta}^m) S_1^2 - (S_2 - \xi_{(i-1)\Delta}^m) S_1 + \frac{1}{2} S_2)}.$$

The parameter  $\sigma^2$  is easier to obtain, as the derivative of the complete log-likelihood leads to the following statistic:

$$(12) \quad S_4 = \frac{1}{n} \sum_{i=0}^n (y_i - f(x_i, \hat{\theta}^{m-1} | \xi^m))^2$$

where conditioning on the hidden process  $\xi^m$  imply a growth-time process given by  $g(x_i, \hat{\theta}^{m-1}) = \int_0^{x_i} \xi_s^m ds$ . Finally, the estimation of parameters  $A, B_0$  and  $b$  is obtained by minimizing the residual sum of squares.

These statistics are then approximated by the stochastic approximation scheme, as in the standard SAEM. Following Ditlevsen and Samson (2014); Lavielle (2014), we choose the form

$$(13) \quad \alpha_m = \begin{cases} 1 & m \leq m_0 \\ (m - m_0)^{-9/10} & m > m_0 \end{cases}$$

for the Stochastic Approximation sequence in eq. (8), where  $m_0$  determines the iteration step wherafter memory from the previous step is included. We obtain approximations of the statistics, for  $k = 1, \dots, 4$ :

$$(14) \quad s_k^{(m)} = s_k^{(m-1)} + \alpha_m (S_k - s_k^{(m-1)}).$$

We then update the parameter estimates in terms of these statistics

$$\begin{aligned} \hat{\rho}^m &= s_1^{(m)}; & \hat{\beta}^m &= -\frac{1}{\Delta} \log(\hat{\rho}^m); & (\hat{\omega}^m)^2 &= s_3^{(m)}; & (\hat{\sigma}^m)^2 &= s_4^{(m)}; \\ \hat{a}^m &= s_2^{(m)} \mathbb{1}_{\{2\hat{a}^0 > s_2^{(m)} > \frac{1}{2}a^0\}} + \hat{a}^{m-1} \left(1 - \mathbb{1}_{\{2\hat{a}^0 > s_2^{(m)} > \frac{1}{2}a^0\}}\right). \end{aligned}$$

Since the number of cycles is proportional to  $a$ , we ensure that the process does not mistake random fluctuations for cycles by restricting estimates of  $a$  to be between half and double of

our initial estimate (using peak detection; see section 3.5). If this condition is fulfilled for the statistic associated with  $a$  we update, otherwise the estimate from the previous step is kept. The update of parameters  $A$ ,  $B_0$  and  $b$  is obtained by minimizing  $S_4$  (substituting  $\hat{\theta}^{m-1}$  by  $\hat{\theta}^m$  and using  $\hat{A}^{m-1}$ ,  $\hat{B}_0^{m-1}$  and  $\hat{b}^{m-1}$ ) using optimisation from the R-package `minpack.LM` (Elzhov et al., 2023).

The SAEM algorithm iterates until some stopping criteria is met. Several rules exist for determining when convergence can be assumed (Sammaknejad, Zhao and Huang, 2019). We used the average relative difference and chose the stopping time as the iteration where this average relative difference falls below a specified threshold value for 10 consecutive iterations. We chose a threshold of  $\frac{1}{100}$  which ensured (empirically; found by simulations) that the majority of the trajectories of the iterative SAEM estimates had stabilized.

To summarize, our algorithm is the following. We first use SMC to filter multiple trajectories of  $\xi$  called particles, using the exact transition density. This algorithm is detailed in Section 3.4. Once the latent process is filtered, we proceed to the stochastic approximation step. In the final maximization (M) step, we update the estimates  $\hat{\theta}^m$ . This procedure reiterates until some stopping criteria is met. The basic estimation procedure, tracing the steps above, is summarized in Algorithm 1. Later we generate confidence intervals for the parameters and other derived quantities. This subsequent step is summarized in Algorithm 3.

---

**Algorithm 1:** Parameter estimation using SAEM and martingale estimating functions

---

**Data:**  $(X, Y) := \{(x_1, y_1), \dots, (x_n, y_n)\}$

**Result:**  $\xi, \hat{\theta} := (\hat{A}, \hat{B}_0, \hat{b}, \hat{a}, \hat{\sigma}^2, \hat{\rho}, \hat{\omega}^2)$

Step (1) Initialize parameters  $\hat{\theta}^0$  and the unknown process  $\xi^0$  (see Section 3.5);

$m \leftarrow 1$  ;

**while** "Stopping criteria" **do**

Step (2) Update  $\xi^m$  given  $\hat{\theta}^{m-1}$  using SMC (Algorithm 2) ;

Step (3) Do the stochastic approximation of statistics  $S_1, \dots, S_4$ ;

Step (4) Update  $\hat{a}^m, \hat{\rho}^m, (\hat{\omega}^2)^m, (\hat{\sigma}^2)^m$  using the statistics  $s_1^{(m)}, \dots, s_4^{(m)}$ ;

Step (5) Update  $\hat{b}^m, \hat{A}^m, \hat{B}_0^m$  by optimizing  $S_4$  ;

$m \leftarrow m + 1$

**end**

---

**3.4. SMC algorithm.** Inside Algorithm 1 we apply SMC to filter out the hidden process  $\xi$ . The SMC algorithm provides a set of  $n_p$  particles  $(\xi_j^{(j)})_{j=1, \dots, n_p}$  and weights  $(W^{(j)})_{j=1, \dots, n_p}$  approximating the conditional smoothing distribution  $p(\xi_0, \dots, \xi_n | y_0, \dots, y_n; \theta)$  (Del Moral, Doucet and Jasra, 2006b; Doucet, De Freitas and Gordon, 2001). The SMC algorithm is an iterative algorithm. At each iteration in time, particles are sampled from a proposal distribution denoted  $q(\xi_i | \xi_{i-1}, y_i, y_{i-1})$ . To ease notation, we denote  $\xi_{0:i} = (\xi_0, \dots, \xi_i)$  and likewise for  $y_{0:i}$ .

We choose the exact transition density  $p(\xi_i | \xi_{i-1})$  introduced in Section 1 as proposal  $q$ . This choice gives a simplified weight equal to

$$(15) \quad W = \frac{p(y_i, \xi_{0:i} | y_{0:i-1}, \theta)}{q(\xi_i | y_i, \xi_{0:i-1}, \theta)} = p(y_i | \xi_i, \theta) \sim \mathcal{N}(f(x_i, \theta), \sigma^2).$$

The algorithm is presented in Algorithm 2 for a given value  $\theta$ . It provides an empirical measure which is an approximation to the smoothing distribution  $p(\xi_{0:n} | y_{0:n}, \theta)$ . A draw from

this empirical distribution can be obtained by sampling an index  $j$  from a multinomial distribution with probabilities  $(W_n^1, \dots, W_n^{n_p})$ .

---

**Algorithm 2:** Sequential Monte Carlo (SMC) - Bootstrap filtering

---

**Data:**  $(X, Y), \theta = (A, B_0, a, b, \sigma^2, \beta, \rho, \omega^2)$

**Result:**  $(\xi^{(j)} = (\xi_0^{(j)}, \dots, \xi_n^{(j)}))_{j=1, \dots, n_p}$

Initialize  $n_p \times n + 1$  matrices  $\xi$  and weights  $W$ , where  $n_p$  is the number of particles; For  $j = 1, \dots, n_p$ , set  $\xi_0^{(j)} = a$  and  $W_0^{(j)} = 1/n_p$ ;

**for**  $i = 1$  **to**  $n$  **do**

Set  $\lambda_i = 2\rho c \xi_{i-1}^{(j)}$  for  $j = 1, \dots, n_p$ ;

Update particles:  $\xi_i^{(j)} \sim \frac{1}{2c} \chi_\nu'^2(\lambda_i)$  for  $j = 1, \dots, n_p$ ;

Compute weights:  $W_i^{(j)} = p(y_j | \xi_i^{(j)}, \theta)$  for  $j = 1, \dots, n_p$  ;

Normalize weights:  $W_i^{(j)} = W_i^{(j)} / \sum_{i=1}^{n_p} W_i^{(j)}$  for  $j = 1, \dots, n_p$  ;

Resample particles by drawing  $n_p$  indices from the set  $\{1, \dots, n_p\}$  with corresponding probabilities

$W_i^{(1)}, \dots, W_i^{(n_p)}$ . Denote the realizations  $\{I_1, \dots, I_{n_p}\}$  and set  $\xi_{0:i}^{(j)} := \xi_{0:I_j}^{(j)}$ ;

**end**

---

In the next two sections we outline the initialization details of step (1) of Algorithm 1 and discuss the bootstrap procedure used to estimate the confidence intervals of the estimates. We end with a section on model validation.

**3.5. Parameter initialization.** Proper initialization will assist SAEM in convergence towards a global optimum. This is particularly important for our problem, since the loss function of the non-linear model (3) is expected to exhibit many local maxima due to the trigonometric functions. Obtaining good initial estimates is a non-trivial task, and typically involves heuristic approaches. Here we present our chosen initialization, denoted  $\hat{\theta}^0$ . The points (1) through (6) are listed in the order they should be performed.

**(1) Peak detection.** In order to identify peaks in the data  $y$ , we apply a locally estimated scatterplot smoothing (LOESS) filter (Cleveland, Grosse and Shyu, 2017), which performs local polynomial regression around each data point by using 10% of the neighboring points. Denote the resulting smoothed data vector  $y_s$ . Then apply a rolling max filter on  $y_s$ , which at each point selects the maximum value within a window of size  $(n/5)\Delta$ . We use the rolling max function in the R-package ZOO (Zeileis and Grothendieck, 2005). Denote the resulting data vector  $y_{max}$ . Our initial guess at the peaks are

$$(16) \quad \{x_1^{*0}, \dots, x_L^{*0}\} = \{x_i + (n/10)\Delta \mid y_{max}(x_i) > y_s(x_i), i = 1, \dots, n\}.$$

Note that the initial number of peaks  $L$  might be different from the true number  $K$ .

**(2) Amplitudes:**  $A, B_0$ . Perform 2-means clustering (using the R function `kmeans`) on the peak values  $y_s(x_1^{*0}), \dots, y_s(x_L^{*0})$  to identify two centroids, HT and LT, representing the mean heights of the high and low peaks. Recall that  $A + B_0$  corresponds to low peaks, and  $B_0 - A$  to high peaks. We can therefore estimate  $\hat{A}^0 = \frac{\text{HT} - \text{LT}}{2}$  and  $\hat{B}_0^0 = \frac{\text{HT} + \text{LT}}{2}$ .

**(3) Frequency:**  $a$ . Assume that the difference between consecutive peak positions correspond to half a cycle, then the cycle period is  $T_l = 2 \times (x_l^{*0} - x_{l-1}^{*0})$  for  $l = 2, \dots, L$ . Estimates of the (angular) frequency is then  $a_l = 2\pi/T_l$  and we choose  $\hat{a}^0 = \text{median}(a_2, \dots, a_L)$ . We

use the median to exclude extreme frequencies, for instance because we included too many peaks, or excluded intermediate peaks.

**(4) Phase:** *b.* Regress half of the data-vector  $y(x_i)$ ,  $x_i < n\Delta/2$ , on  $f(x)$  in (3) with only  $b$  as a free parameter, fixing  $A = \hat{A}^0$ ,  $B_0 = \hat{B}_0^0$  and  $\xi_x = \hat{a}^0$  (no stochastic process) for all  $x$ . We use non-linear least squares in the R-package `minpack.lm` (Elzhov et al., 2023). Limiting the analysis to the first half of the observations makes the assumption of a constant frequency  $\xi_x = a$  for all  $x$  less contentious. The initial estimate  $\hat{b}^0$  is then the estimated parameter from the regression.

**(5) Measurement error:**  $\sigma^2$ . The variance of the measurement noise is approximated from the smoothed signal  $y_s$  from the peak detection, setting  $(\hat{\sigma}^2)^0 = \frac{1}{n} \sum_{i=1}^n (y(x_i) - y_s(x_i))^2$ .

**(6) Hidden process parameters:**  $\rho, \omega$ . Make a grid of plausible values for  $\rho$  and  $\omega^2$ . Specifically, we consider all 28 combinations of  $\rho \in (0.35, 0.45, 0.55, 0.65, 0.75, 0.85, 0.95)$  and  $\omega^2 \in (0.4, 0.8, 1.2, 1.6) \times \hat{a}^0 \beta$ , where  $\beta = -\frac{1}{\Delta} \log \rho$ . We then run SMC (Algorithm 2) with a fixed number of particles  $n_p$  for each combination, giving a total of  $28 n_p$  SMC particles. We resample among the  $28 n_p$  particles at each step and select a final candidate based on the final weights. The selected particle is then our initial estimate  $(\hat{\rho}^0, (\hat{\omega}^2)^0)$ .

**3.6. Bootstrapping.** Standard errors and confidence intervals for all parameters estimated using SAEM (Algorithm 1) are computed using residual block bootstrapping. The general procedure is described in Algorithm 3.

---

**Algorithm 3:** Residual block bootstrapping

---

**Data:** Observations  $y = (y_1, \dots, y_n)$  and fitted values  $\hat{y} = (\hat{y}_1, \dots, \hat{y}_n)$

**Result:** Vector of estimates  $(\hat{\theta}_j)_{j=1, \dots, M}$

$j \leftarrow 1$  ;

Set number of bootstrap replications  $M \leftarrow M_0$  ;

**while**  $j < M$  **do**

Step (1) Compute residuals  $r = y - \hat{y}$ ;

Step (2) Define number of blocks  $n_b = n^{1/3}$  and block size  $bs := \left\lfloor \frac{n}{n_b} \right\rfloor$  ;

Step (3) Define overlapping blocks of residuals  $[r_i, r_{i+bs}], i = 1, \dots, n - bs$  ;

Step (4) Construct bootstrapped residuals  $r^{(j)}$  by sampling  $\lceil n_b \rceil$  random blocks of residuals. Then trim  $r^{(j)}$  to length  $n$  ;

Step (5) Construct bootstrapped signal as  $y^{(j)} = \hat{y} + r^{(j)}$ ;

Step (6) Estimate  $\hat{\theta}_j$  using Algorithm 1 on  $y^{(j)}$  ;

$j \leftarrow j + 1$

**end**

---

[TODO: Insert comment and reference about number of blocks used.] In Step (1) of Algorithm 3 we sample data directly from the model (1), (3), (4) with estimated parameters  $\hat{\theta}$ . This means that  $y_i^{(j)} = \hat{f}(x_i) + \epsilon_i^{(j)}$  where  $\epsilon_i^{(j)} \sim \mathcal{N}(0, \hat{\sigma}^2)$ .

**3.7. Model validation.** To assess the quality of our model, we consider the raw residuals defined as

$$(17) \quad \text{res}_i = y_i - \hat{y}_i$$

where  $\hat{y}_i$  is the fitted value of observation  $i$ . We use the (raw) residuals to validate the mean structure and homoscedasticity assumption using the residual plot. Additionally, we compare the (raw) empirical residuals, equation (17), with simulated residuals (from data generated under the fitted model). This allows us to assess how well the model's residuals reflect the variability and distributional assumptions implied by the model.

To address the estimator variability and bias, we computed the (vector of) relative difference(s) ( $\text{true parameter} - \text{estimated parameter}$ )/ $\text{true parameter}$  for all parameters, except for the phase  $b$ . For the phase parameter  $b$ , we instead computed the smallest absolute difference on the unit circle. For the case-study, we applied Algorithm 3 and produced several bootstrap estimates  $\tilde{\theta}_j$ ,  $j = 1, \dots, M$ . We then considered differences between the estimated and bootstrapped versions:  $(\hat{\theta} - \tilde{\theta}_j)/\hat{\theta}$ . In the simulation study, where parameters  $\theta_m$  are known a priori for each signal  $m$ , we considered the difference between estimated and true parameters:  $(\theta_m - \hat{\theta}_j)/\theta_m$ .

**4. Simulation study.** A total of 400 signals was simulated, with a fixed step size equal to  $\Delta x = x_i - x_{i-1} = 0.1$ . Below, we describe how parameters were selected. For now, assume all parameters are known. To obtain the hidden stochastic process, the solution to equation (4), we used the exact transition density (described in Section 2) to simulate a trajectory starting with  $\xi_0 = 0$ . We then obtained  $g(x_i) = \sum_{j=1}^i \xi_j \Delta$ . Finally, we sampled a signal using (1) and (3).

For the first  $M = 200$  simulations, the parameters were fixed at values shared by all signals. These parameters were chosen to best reproduce the real signals of the case study. For each simulated signal  $m$ , we computed the relative differences between any true parameter  $\theta_m$  and its estimate  $\hat{\theta}_m$  (Figure 3) defined as  $(\theta_m - \hat{\theta}_m)/\theta_m$ . We included the number of cycles to measure how well the model predicts the number of peaks in the signal. The violinplots in Figure 3 show how the estimates deviate from the true parameters relative to their scale. From the figure, we see that  $\rho$  displays some variability, but without a prominent bias, suggesting that the rate of adjustment of the growth-time process could be hard to identify. Similarly, the amplitude parameters  $A$ ,  $B_0$  and the phase  $b$  show a sizeable variability, without a clear bias. For the remaining parameters, there are no substantial bias, and a more dense concentration of the estimates around their true values. Most importantly, the baseline frequency  $a$  and the number of cycles (used as a proxy for how well the model describes the periodic signal) display a low variance and a low bias.

For the other  $M = 200$  simulations, we allowed the parameters to vary between signals, in order to more deeply explore how well our method identifies the number of cycles, and to which extent it deviates over a variety of signals and parameter configurations (Figure 4). The signal length  $n$  was sampled with uniform probability between one of four options: 200 (short), 400 (medium short), 600 (medium long), 800 (long). We then set the minimum number of cycles  $C_{min} = 2$  and the maximum number of cycles  $C_{max} = \max(6, n/100 \times 1.5)$ , i.e., 6, 9 or 12 cycles. We let  $a_{min} = 2\pi C_{min}/n\Delta$  and  $a_{max} = 2\pi C_{max}/n\Delta$ . The sampling distributions of the other parameters were uniformly distributed  $\mathcal{U}$  as

$$(18) \quad \rho \sim \mathcal{U}(0.55, 0.95), \quad \beta = -\frac{1}{\Delta} \log(\rho), \quad \sigma \sim \mathcal{U}(0.1, 0.5),$$

$$(19) \quad A \sim \mathcal{U}(0.4, 0.6), \quad B_0 \sim \mathcal{U}(0.6, 1), \quad a \sim \mathcal{U}(a_{min}, a_{max})$$

$$(20) \quad b \sim \mathcal{U}(0, 2\pi), \quad \omega \sim \mathcal{U}(0.3, 0.8) \sqrt{2a\beta}$$

The support of the uniform distributions were inspired by estimates from the case-study signals, and by considering the visual appearance of different parameter configurations. The

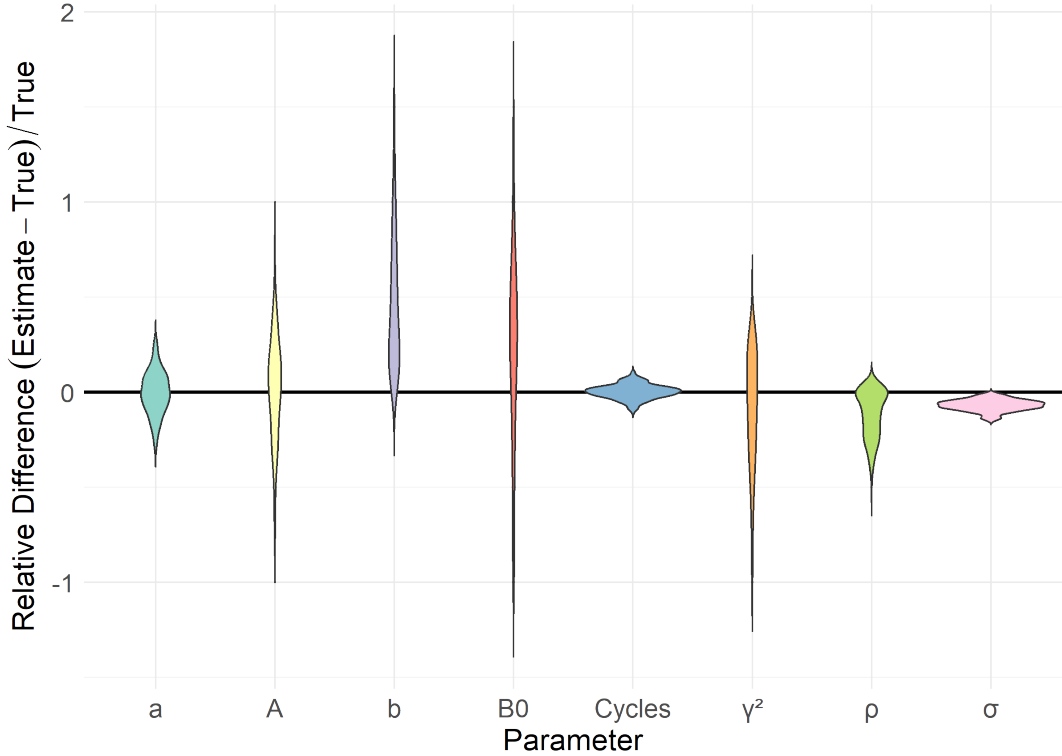


**Fig 3: Estimator variability.**  $M = 200$  simulations with fixed parameters  $n = 500$ ,  $\rho = 0.9$ ,  $\sigma^2 = 0.09$ ,  $A = 0.5$ ,  $B_0 = 0.8$ ,  $a = 0.5$ ,  $b = \frac{\pi}{2}$ ,  $\omega^2 = 1$ . The relative difference  $(\theta_m - \hat{\theta}_m)/\theta_m$ ,  $m = 1, \dots, 200$  of parameter estimates  $\hat{\theta}_m$  obtained from signals simulated with parameter  $\theta_m$ . Included are all parameters, and the number of cycles are computed with formula (5). For  $b$  we computed the smallest absolute relative difference on the unit circle, since there are no principal direction.

result of this second part of the simulation is displayed in Figure 4 which shows that 92% of the estimates fall within 1 cycle from the true number of cycles, and less than 1% deviate by more than 3 cycles.

An example of a simulated signal is presented in the top plot of Figure 5, which also displays the model fit. In the second row of Figure 5 we have provided visualizations of the hidden process  $(\xi_x)_{x \geq 0}$  associated with the simulated signal, both the actual process and the estimated version. The third row of Figure 5 displays the growth-time process  $\hat{g}(x)$ , along with its estimated counterpart, obtained through the integration of  $(\hat{\xi}_x)_{x \geq 0}$ .

**5. Age determination of a narwhal tusk.** Narwhals exhibit a consistent and well-documented annual migration pattern as they move between specific summer and winter habitats, which are situated in fjords and inlets, and offshore areas, respectively (Heide-Jørgensen et al., 2020). The primary prey items consist of halibut, squids, and polar cod (Laidre and Heide-Jørgensen, 2005; Watt and Ferguson, 2014). On their seasonal migration routes, the narwhals travel through the same regional water masses to and from summer- and winter grounds. The strict diet and rigid migration pattern results in distinguishable GLGs, the annual depositions of growth layers in the dentin zone of the tusk, consisting of an opaque and a translucent layer, see Figure 6b. Continuous fluctuations in the deposition/biomineralization

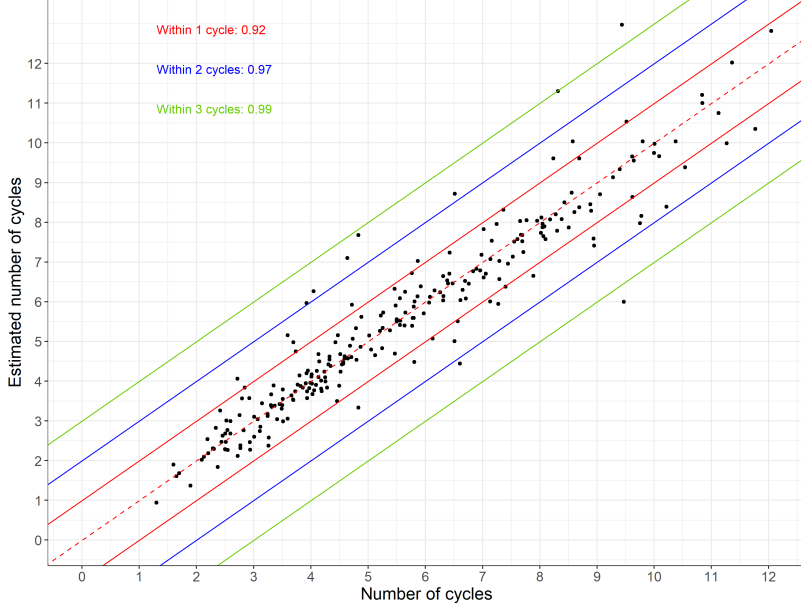


**Fig 4: Estimated number of cycles against true number of cycles.** Red, blue and green ribbons enclose estimates of number of cycles from simulated data sets with less than 1, 2, and 3 cycles of deviation from the true number of cycles, respectively.

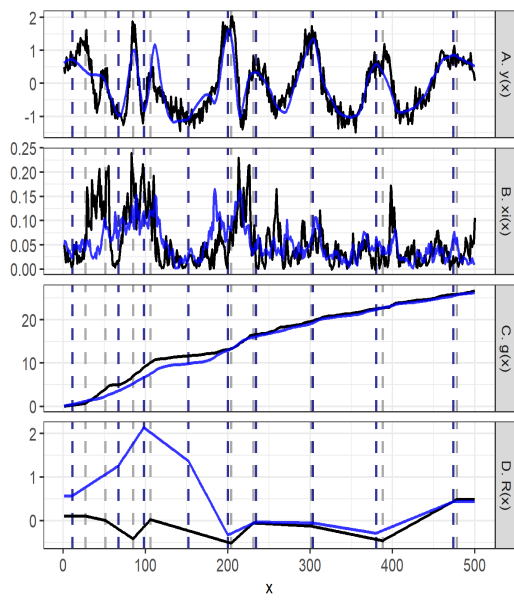


**Fig 5: Simulated and fitted signal.** Simulated signals are in black, fitted signals in blue. The data set was simulated using  $n = 500$ ,  $\Delta = 1$ ,  $\rho = 0.82$ ,  $\beta = 0.2$ ,  $\sigma^2 = 0.04$ ,  $A = 0.5$ ,  $B_0 = 0.8$ ,  $a = 0.05$ ,  $b = \pi/2$ ,  $\omega^2 = 0.01$ . The amplitude displacement parameters  $r_k$  were simulated from a zero-mean normal distribution with variance 0.25. The SAEM-SMC algorithm used  $n_p = 500$  number of particles. A. Simulated signal and fitted signal. B. Simulated hidden process  $(\xi_x)_{x \geq 0}$  and estimate  $(\hat{\xi}_x)_{x \geq 0}$ . C. Simulated growth time process  $g(x)$  and estimate  $\hat{g}(x)$ . D. Amplitude correction function  $R(x)$  and estimate  $\hat{R}(x)$ . Gray dashed lines are (true) signal peaks. Blue dashed lines are estimated signal peaks.

rates show up in the signals and likely occur due to seasonal variations driven by environmental factors, such as temperature or salinity (Hüssy et al., 2021b). In addition, the physiological characteristics of the animals, notably age and health, likely modulate metabolic processes and as a result potentially influence the biomineralization rate (Mosegaard, Svedäng and Taberman, 1988; Hüssy and Mosegaard, 2004). These assumptions are based on otolith studies, and it seems reasonable to assume that the tusk growth rate exhibit similar characteristics. The recurring deposition of GLGs in conjunction with a variable deposition rate produces a cyclic profile that fits well into our working model (1). Since the hypothesis is that one GLG is deposited annually, counting these cycles will provide an age estimate of the narwhal. An approximate determination of the range of GLGs in a tusk piece can be made

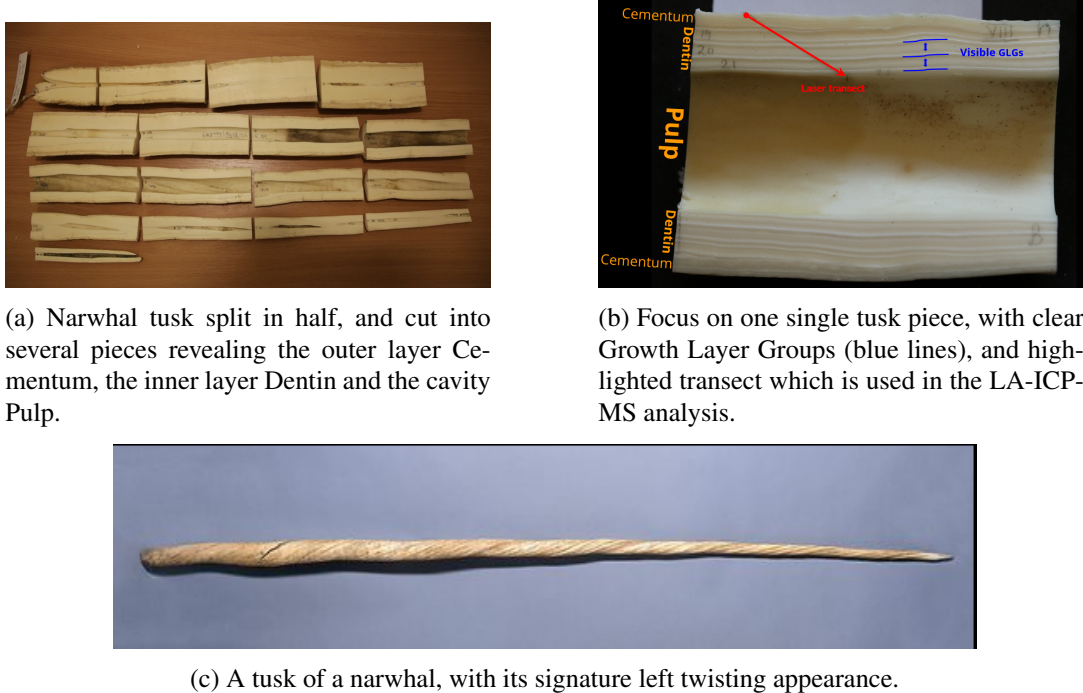
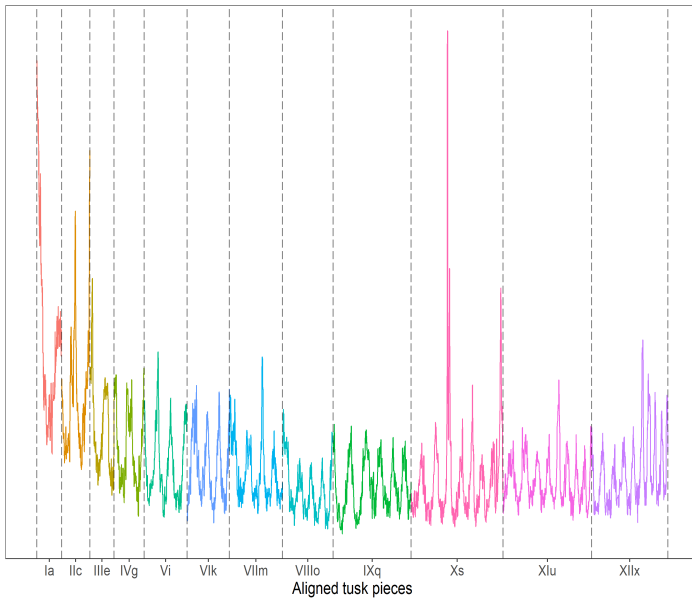


Fig 6: **Tusk and tusk pieces.**

through visual observation, see Figure 6b. However, the visual counts are highly uncertain for some tusk pieces, and automatic robust methods based on more objective criteria and quantitative measures are needed.

**5.1. Data acquisition and preparation.** We analyzed one tusk (ID 956) collected from the Inuit Hunt of narwhals in Niaqornat, West Greenland, in 2010. The tusk was sectioned in two halves and one was used for subsequent analysis. The half tusk were divided into several tusk pieces covering all GLGs (see Figure 6a). This resulted in 12 pieces. Each tusk piece was measured along a transect (see Figure 6b) using Laser Ablation Inductively Coupled Plasma Mass Spectrometry (LA-ICP-MS) by the Geological Survey of Denmark and Greenland (GEUS), providing the concentrations of 14 isotopes and trace elements (Sr, Ba, Zn, Mg, K, Li, Mn, Pb, Cu, P, Ti, Cr, Co, Rb) (Thomsen et al., 2022; Koch and Günther, 2011). Our analysis centers on Barium-137 normalized by the isotope Calcium-43 in high abundance, since among the set of elements, Barium displayed distinct cyclic patterns speculated to correlate with migration between summer and winter grounds (Heimbrand et al., 2020; Limburg et al., 2011). Consequently two peaks in the signal would correspond to one annual cycle. The combined signal over all pieces displaying the cyclic pattern is visualized for tusk 956 in Figure 7.

**5.2. Dating the observations.** For each piece  $j$  of the tusk, we fit the model with Algorithm 1 (subpanel A in Figure 8 and Figure 9). We fit each tusk piece individually allowing different parameter values in each, since the values will depend on the angle of the transect line (see red line in Figure 6b) across the piece. For example, a steeper line will increase the length of a year, changing the distance scale, which will change all parameters related to the growth process. Likewise, amplitudes are expected to change over the lifetime of the



**Fig 7: Analyzed data set.** Calcium-43 adjusted Barium-137 signals obtained from tusk 956. The data set consists of 12 piecewise signals merged together into one common time series in chronological order. The first part of the time series corresponds to the tip of the tusk, deposited when the whale was born, and the last part of the series corresponds to the base nearest the skull, deposited just before death.

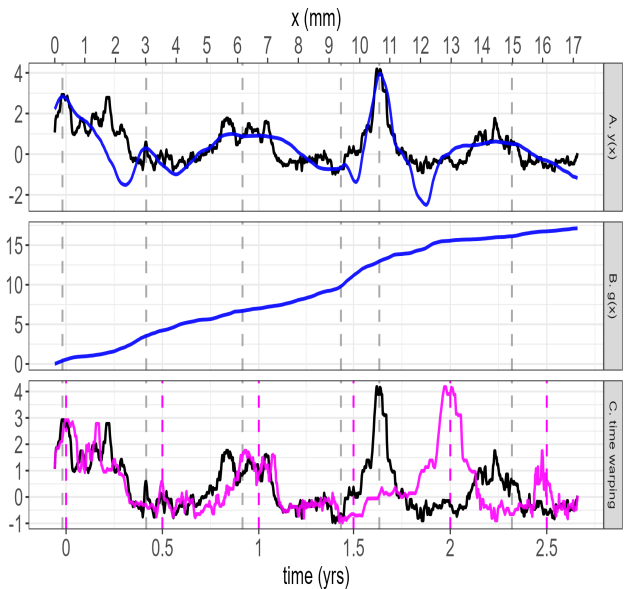


**Fig 8: Time warping of barium signal in narwhal tusk for piece 956-VII.** A. Fitted signal (blue curve) and true signal (black curve). B. Estimate  $\hat{g}(x)$  of the growth time process  $g(x)$ . C. Transformation from measured distance  $x$  (black curve, same as in panel A) to estimated time  $t$  (time warping, magenta curve). Blue dashed lines are the estimated peaks found with equation (??). Magenta dashed lines are the warped peaks. The horizontal axis is displayed both in years (lower axis) and mm (distance on tusk; upper axis).

animal, and thus, change from piece to piece. We obtain estimates of the growth time processes  $\hat{g}_j(x_{ij})$ ,  $i = 1, \dots, n_j$ ,  $j = 1, \dots, 12$ , where  $n_j$  are the number of observations in piece  $j$  (Figure 8B). This takes us from the original coordinates  $(y_{ij}, x_{ij})_{i=1, \dots, n_j, j=1, \dots, 12}$  to a new set of coordinates  $(y_{ij}, t_{ij})$  with  $t_{ij} = \hat{g}_j(x_{ij})$ , where  $t_{ij}$  is a increasing sequence proportional to the number of cycles. This shift in coordinates warps the signal and adjust for any non-linearity present in the original time line (Figure 8C).

For each of the 12 pieces, we obtain a growth time process  $\hat{g}_j(x_{ij})$ . The total number of observations is  $n_{tot} = \sum_{j=1}^{12} n_j$ . Re-enumerate the set of indices by concatenating chrono-

TABLE 2

*Age estimates (total GLGs) with 95% confidence interval. \* Based on radiocarbon dating using the bomb pulse (Zoppi et al., 2004) and Carbon-14 measurements from the narwhal tusk (Garde et al., 2024).*

Tusk ID	Age (estimate)	Age (confidence interval)	GLGs (manual count)	Age ( $^{14}\text{C}$ count)*
956	51	44 - 60	57	54

logically

$$(21) \quad ij \rightarrow m = i + \sum_{l=1}^j n_l, \quad m = 1, \dots, n_{tot}$$

Assuming each piece signal can be glued together, without any gap in the timeline, we can then construct an *aggregated growth time process*:

$$(22) \quad \hat{g}(x_m) = \hat{g}(x_{ij}) = \begin{cases} \hat{g}_1(x_{i1}) & i \leq n_1 \\ \hat{g}_{j-1}(x_{n_{j-1}, j-1}) + \hat{g}_j(x_{ij}) & n_{j-1} < i \leq n_j, j = 2, \dots, 12 \end{cases}$$

One revolution around the unit circle corresponds to one annual cycle. Thus, the number of elapsed years at observation  $m$  is  $\hat{g}(x_m)/2\pi$ , see eq. (5). Since we know the time of death of the narwhal (in this case 2010), we date each observation  $m$  by

$$(23) \quad \text{Year}(m) = 2010 - (\hat{g}(x_n) - \hat{g}(x_m)) / 2\pi, \quad m = 1, \dots, n_{tot}$$

**5.3. Age estimation.** The quantity of interest is the age of the narwhal, which is equivalent to the number of cycles easily obtained using formula (5) and  $\hat{g}(x_m)$ . A confidence interval is obtained by bootstrapping (Algorithm 3).

This is accomplished by performing parametric bootstrapping on each piece, and combine the bootstrapped signals randomly to produce  $M = 10^7$  realizations of aggregated growth-time processes  $\hat{g}(x_m)$ , of which each has its own age estimate.

The age estimate (number of GLGs), including upper and lower confidence bound, are summarized in table 2.

**5.4. Model validation.** We have overlain the fitted curves with the tusk pieces, to compare the identified peaks with the GLGs of the tusks. In Figure 9 we show two of such examples. The laser line is highlighted in green and red, when inside and outside the dentin area, respectively. The positions of the peaks are marked with vertical red lines, and we can discern how these peaks appear to align with consecutive white lines, which presumably represent one GLG. A more formal model validation was carried out by inspecting the residuals (defined in Section 3.7) visualized in Figure 10. The left plot shows a residual plot (raw residuals against fitted values) for each of the 12 fitted signals and the right column display a QQ-plot, where raw residuals are compared against simulated residuals. The residual plots reveal a skewed pattern for several tusk pieces, likely caused by rapid secondary cycles unique to our case study signals, which are not incorporated in our model (1). See the raw signal in Figure 8 for an illustration of these secondary cycles. For the QQ-plots, most residuals are symmetrically distributed around the diagonal, indicating that the central tendencies are well-captured by the model. However, skewed behavior in the tails, such as in piece Xs, suggests that the model may not fully capture the behavior of extreme values, possibly due to increased variability in regions where the signal has peaks.

Estimator uncertainties within each tusk piece is visualized in Figure 11 using violinplots for all parameters. The procedure is described in section 3.7. The simulated signals generally

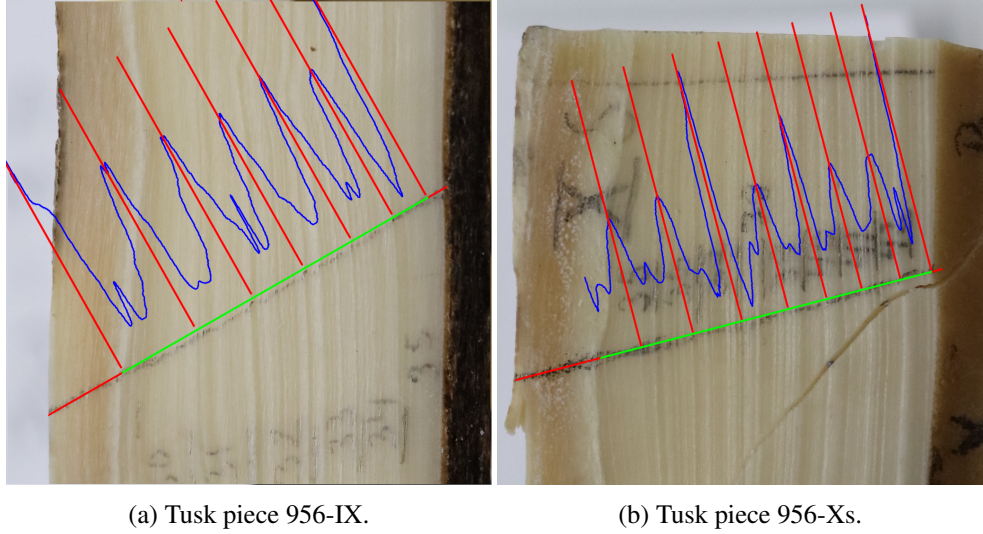


**Fig 9: Fitted signals overlain tusk pieces.** Two tusk pieces with fitted signals (blue lines), estimated placement of high peaks (red vertical lines), laser line in dentin region (green segment) and pulp/cementum region (red segments).

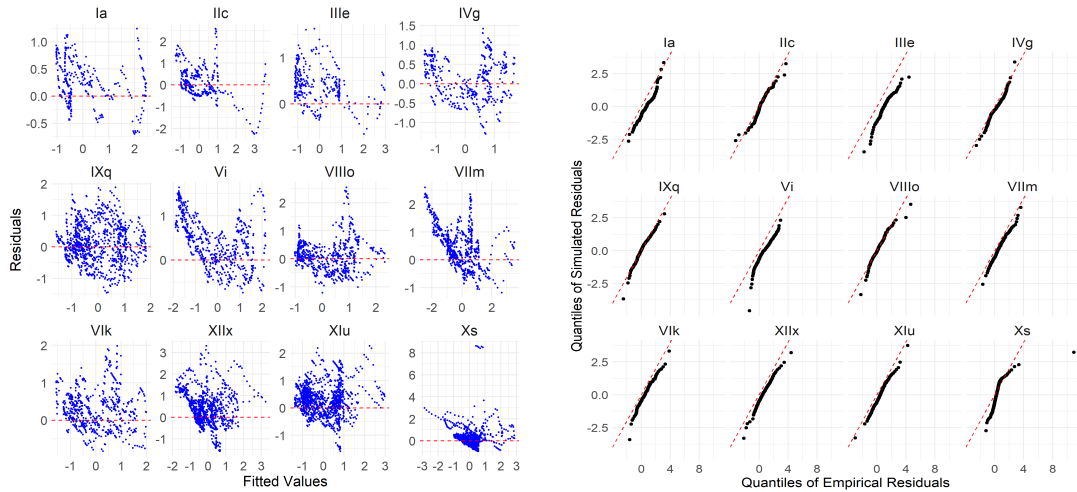


**Fig 10: Model validation plots for the case-study signals.** Residual plots (left) and QQ-plots (right) for all 12 signals of tusk 956.

result in consistent estimates for parameters  $a, \gamma^2$ , which centers around the model estimates of the original signals. However, among the 12 signals used in the case study, Figure 11 also reveals some spurious discoveries. Several estimators display both a sizeable amount of variability and bias. For example, the one-lag autocorrelation  $\rho$  is highly variable and for a few signals also show a slight bias. The noise  $\sigma$  is drastically underestimated at the early pieces, which exhibit few cycles, and slightly overestimated at later pieces, which contain more cycles. The phase  $b$  also displays a high variance, and appears unidentifiable.

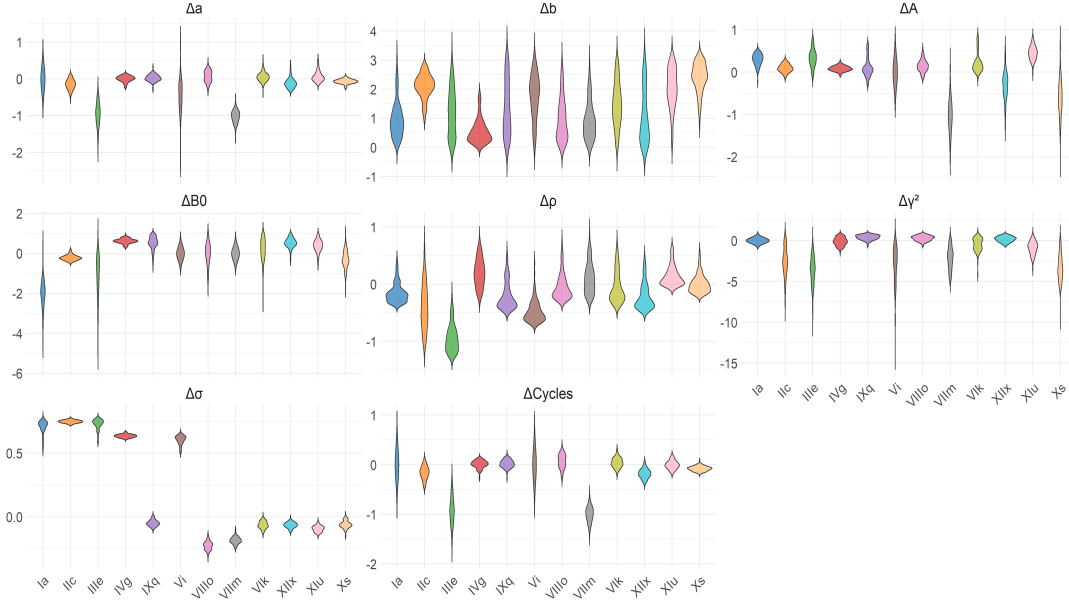


**Fig 11: Estimator variability of tusk 956.** The x-axis represent the different tusk pieces (12 in total). For an estimate  $\hat{\theta}$  of some model parameter  $\theta$  we compute 100 bootstrap estimates  $\tilde{\theta}$  and plot the differences  $\Delta\theta := (\hat{\theta} - \tilde{\theta})/\hat{\theta}$ . The difference in phase  $\Delta b$  is computed as the shortest distance on the unit circle, not in absolute difference, thus all differences are non-negative.

**6. Discussion and research outlook.** The main attraction of the model is arguably the identification of the growth time process  $g(x_i) = \int_{s=0}^{x_i} \xi_s ds$  which effectively translates into identification of the timeline of the underlying hidden process (4) driving the changing periodicity. While the process  $(\xi_x)_{x \geq 0}$  is difficult to infer, the integrated process  $g(x_i)$  appear to be well identified. The estimators of the process mean  $a$  and the stationary variance  $\gamma^2$  are also well identified, but the one-lag variance  $\rho$  seemed slightly harder to identify, likely caused by the integration of the process.

It is important to consider the interplay between frequency and amplitude. For any periodic signal, we need to determine whether changes are primarily driven by variations in amplitude (i.e. magnitude of the signal) or frequency (i.e. rate of the signal). In this study, we assumed that any instantaneous jumps in the signal are due to changes in frequency, whereas the amplitudes are slowly varying. For the narwhal tusks, this assumption means that rapid changes in the signal occur due to changes in growth rate rather than fluctuations in the uptake of elements in the tusk. Assuming slowly varying amplitudes, we detected any changes and ensured the signal remained consistent with the constant-amplitude assumption during preprocessing.

While we believe our presented model to be both flexible and theoretically sound, the practical implementation still requires some choices which should be tailored to the specific signals. Some examples include selection of smoothing parameters in the initialization phase, runtime parameters (number of iterations inside Algorithm 1, particles in SMC and the threshold for the stopping criteria). These choices do not only assist the method in proper convergence, but are also important for controlling algorithmic runtime. These choices should not be perceived as weaknesses within our model but rather as strategic responses that will serve the algorithm in producing more reliable estimates and guide the optimization procedure.

**Acknowledgments.** We would like to thank the Greenlandic hunters for providing the narwhal tusk, Jeppe Møhl for sectioning the tusk, and Tonny Bernt Thomsen and Benjamin Heredia at the Geological Survey of Denmark and Greenland for performing the elemental analyses. The tusk was imported to Denmark from Greenland on CITES import permit no. IM 0822-296/18. Finally, we would like to thank Adam Gorm Hoffman, who was working with modelling and data analysis of a narwhal tusk in the early stage of the project.

**Funding.** This work has received funding by Novo Nordisk Foundation NNF20OC0062958; by NordForsk (Grant number 105053), and by the French-Danish CNRS International Research Network MaDeF IRN.

## REFERENCES

- AMAIIS, R. S., MOREAU, P. S., FRANCISCHINI, D. S., MAGNUSSON, R., LOCOSSELLI, G. M., GODOY-VEIGA, M., CECCANTINI, G., RODRIGUEZ, D. R. O., TOMAZELLO-FILHO, M. and ARRUDA, M. A. (2021). Trace elements distribution in tropical tree rings through high-resolution imaging using LA-ICP-MS analysis. *Journal of Trace Elements in Medicine and Biology* **68** 126872.
- BIBBY, B. M. and SØRENSEN, M. (1995). Martingale estimation functions for discretely observed diffusion processes. *Bernoulli* 17–39.
- CHARLES, C. D., LYNCH-STIEGLITZ, J., NINNEMANN, U. S. and FAIRBANKS, R. G. (1996). Climate connections between the hemisphere revealed by deep sea sediment core/ice core correlations. *Earth and Planetary Science Letters* **142** 19–27.
- CLEVELAND, W. S., GROSSE, E. and SHYU, W. M. (2017). Local regression models. In *Statistical models in S* 309–376. Routledge.
- CLEVELAND, R. B., CLEVELAND, W. S., MCRAE, J. E. and TERPENNING, I. (1990). STL: A seasonal-trend decomposition. *J. Off. Stat.* **6** 3–73.
- DAGUM, E. (2013). Time Series Modelling and Decomposition. *Statistica* **70**. <https://doi.org/10.6092/issn.1973-2201/3597>
- DEL MORAL, P., DOUCET, A. and JASRA, A. (2006a). Sequential monte carlo samplers. *Journal of the Royal Statistical Society Series B: Statistical Methodology* **68** 411–436.
- DEL MORAL, P., DOUCET, A. and JASRA, A. (2006b). Sequential monte carlo samplers. *Journal of the Royal Statistical Society Series B: Statistical Methodology* **68** 411–436.
- DELYON, B., LAVIELLE, M. and MOULINES, E. (1999). Convergence of a stochastic approximation version of EM algorithm. *The Annals of Statistics* **27** 94–.
- DEMPSTER, A. P., LAIRD, N. M. and RUBIN, D. B. (1977). Maximum Likelihood from Incomplete Data via the EM Algorithm. *Journal of the Royal Statistical Society. Series B (Methodological)* **39** 1–38.
- DITLEVSEN, S. and LANSKY, P. (2006). Estimation of the input parameters in the Feller neuronal model. *Phys. Rev. E* **73** 061910. <https://doi.org/10.1103/PhysRevE.73.061910>
- DITLEVSEN, S., RUBIO, A. C. and LANSKY, P. (2020). Transient dynamics of Pearson diffusions facilitates estimation of rate parameters. *Communications in nonlinear science and numerical simulation* **82**. <https://doi.org/10.1016/j.cnsns.2019.105034>
- DITLEVSEN, S. and SAMSON, A. (2014). Estimation in the partially observed stochastic Morris-Lecar neuronal model with particle filter and stochastic approximation methods. *Annals of Applied Statistics* **8** 674–702. <https://doi.org/10.1214/14-AOAS729>
- DOUCET, A., DE FREITAS, N. and GORDON, N. (2001). An introduction to sequential Monte Carlo methods. *Sequential Monte Carlo methods in practice* 3–14.
- ELZHOV, T. V., MULLEN, K. M., SPIESS, A.-N. and BOLKER, B. (2023). minpack.lm: R Interface to the Levenberg-Marquardt Nonlinear Least-Squares Algorithm Found in MINPACK, Plus Support for Bounds R package version 4.2.1.
- GARDE, E., DITLEVSEN, S., OLSEN, J. and HEIDE-JØRGENSEN, M. P. (2024). A radiocarbon bomb pulse model for estimating the age of North Atlantic cetaceans. *Biology Letters* 1–19. In press.
- GLASS, L. and MACKEY, M. C. (1988). *From Clocks to Chaos: The Rhythms of Life*. Princeton University Press.
- HEIDE-JØRGENSEN, M. P., BLACKWELL, S. B., WILLIAMS, T. M., SINDING, M. H. S., SKOVRIND, M., TERVO, O. M., GARDE, E., HANSEN, R. G., NIELSEN, N. H., NGÔ, M. C. and DITLEVSEN, S. (2020). Some like it cold: Temperature-dependent habitat selection by narwhals. *Ecology and Evolution* **10** 8073–8090. <https://doi.org/10.1002/ece3.6464>

- HEIMBRAND, Y., LIMBURG, K. E., HÜSSY, K., CASINI, M., SJÖBERG, R., PALMÉN BRATT, A.-M., LEVINSKY, S.-E., KARPUSHEVSKAIA, A., RADTKE, K. and ÖHLUND, J. (2020). Seeking the true time: Exploring otolith chemistry as an age-determination tool. *Journal of Fish Biology* **97** 552–565. <https://doi.org/10.1111/jfb.14422>
- HÜSSY, K. and MOSEGAARD, H. (2004). Atlantic cod (*Gadus morhua*) growth and otolith accretion characteristics modelled in a bioenergetics context. *Canadian Journal of Fisheries and Aquatic Sciences* **61** 1021–1031.
- HÜSSY, K., KRÜGER-JOHNSEN, M., THOMSEN, T. B., HEREDIA, B. D., NÆRAA, T., LIMBURG, K. E., HEIMBRAND, Y., MCQUEEN, K., HAASE, S., KRUMME, U. et al. (2021a). It's elemental, my dear Watson: validating seasonal patterns in otolith chemical chronologies. *Canadian Journal of Fisheries and Aquatic Sciences* **78** 551–566.
- HÜSSY, K., LIMBURG, K. E., DE PONTUAL, H., THOMAS, O. R., COOK, P. K., HEIMBRAND, Y., BLASS, M. and STURROCK, A. M. (2021b). Trace element patterns in otoliths: the role of biomimetic mineralization. *Reviews in Fisheries Science & Aquaculture* **29** 445–477.
- JANK, W. (2006). Implementing and Diagnosing the Stochastic Approximation EM Algorithm. *Journal of Computational and Graphical Statistics* **15** 803–829.
- JEONG, Y.-S., JEONG, M. K. and OMITAOUMO, O. A. (2011). Weighted dynamic time warping for time series classification. *Pattern recognition* **44** 2231–2240.
- JOUZEL, J. and MASSON-DELMOTTE, V. (2010). Paleoclimates: what do we learn from deep ice cores? *Wiley Interdisciplinary Reviews: Climate Change* **1** 654–669.
- KOCH, J. and GÜNTHER, D. (2011). Review of the state-of-the-art of laser ablation inductively coupled plasma mass spectrometry. *Applied Spectroscopy* **65** 155A–162A.
- LAIDRE, K. L. and HEIDE-JØRGENSEN, M. P. (2005). Winter feeding intensity of narwhals (*Monodon monoceros*). *Marine Mammal Science* **21** 45–57. <https://doi.org/10.1111/j.1748-7692.2005.tb01207.x>
- LAVIELLE, M. (2014). *Mixed effects models for the population approach: models, tasks, methods and tools*. CRC press.
- LIMBURG, K., OLSON, C., WALTHER, Y., DALE, D., SLOMP, C. P. and HØIE, H. (2011). Tracking Baltic hypoxia and cod migration over millennia with natural tags. *Proceedings of the National Academy of Sciences of the United States of America* **108** E177–82. <https://doi.org/10.1073/pnas.1100684108>
- MONSERUD, R. A. and MARSHALL, J. D. (2001). Time-series analysis of  $\delta^{13}\text{C}$  from tree rings. I. Time trends and autocorrelation. *Tree Physiology* **21** 1087–1102.
- MOSBACHER, J. B., MICHELSSEN, A., STELVIG, M., HENDRICHSEN, D. K. and SCHMIDT, N. M. (2016). Show me your rump hair and I will tell you what you ate—the dietary history of muskoxen (*Ovibos moschatus*) revealed by sequential stable isotope analysis of guard hairs. *PLoS One* **11** e0152874.
- MOSEGAARD, H., SVEDÄNG, H. and TABERMAN, K. (1988). Uncoupling of Somatic and Otolith Growth Rates in Arctic Char (*Salvelinus alpinus*) as an Effect of Differences in Temperature Response. *Canadian Journal of Fisheries and Aquatic Sciences* **45** 1514–1524. <https://doi.org/10.1139/f88-180>
- SALVADOR, S. and CHAN, P. (2007). Toward accurate dynamic time warping in linear time and space. *Intelligent Data Analysis* **11** 561–580.
- SAMMAKNEJAD, N., ZHAO, Y. and HUANG, B. (2019). A review of the Expectation Maximization algorithm in data-driven process identification. *Journal of Process Control* **73** 123–136. <https://doi.org/10.1016/j.jprocont.2018.12.010>
- SHUMWAY, R. H. and STOFFER, D. S. (2017). *Time Series Analysis and Its Applications: With R Examples*, 4th ed. Springer.
- SØRENSEN, M. (2012). *Statistical Methods for Stochastic Differential Equations* Estimating functions for diffusion type processes. Chapman and Hall/CRC.
- STOUNBERG, J., THOMSEN, T. B., HEREDIA, B. D. and HÜSSY, K. (2022). Eyes and ears: A comparative approach linking the chemical composition of cod otoliths and eye lenses. *Journal of Fish Biology* **101** 985–995.
- THOMSEN, T., KEULEN, N., HEREDIA, B. and MALKKI, S. (2022). *Cannon balls from Bremervörde (D). A characterization of historic cannon balls using SEM and LA-ICPMS microchemistry*. Danmarks og Grønlands Geologiske Undersøgelse Rapport **2022**. GEUS. <https://doi.org/10.22008/gpub/34640>
- WANG, Y., MILLER, D. J., POSKANZER, K., WANG, Y., TIAN, L. and YU, G. (2016). Graphical time warping for joint alignment of multiple curves. *Advances in Neural Information Processing Systems* **29**.
- WATT, C. and FERGUSON, S. (2014). Fatty acids and stable isotopes ( $\delta^{13}\text{C}$  and  $\delta^{15}\text{N}$ ) reveal temporal changes in narwhal (*Monodon monoceros*) diet linked to migration patterns. *Marine Mammal Science* **31**. <https://doi.org/10.1111/mms.12131>
- WOOLLER, M. J., BATAILLE, C., DRUCKENMILLER, P., ERICKSON, G. M., GROVES, P., HAUBENSTOCK, N., HOWE, T., IRGEHER, J., MANN, D., MOON, K. et al. (2021). Lifetime mobility of an Arctic woolly mammoth. *Science* **373** 806–808.

- ZEILEIS, A. and GROTHENDIECK, G. (2005). zoo: S3 Infrastructure for Regular and Irregular Time Series. *Journal of Statistical Software* **14** 1–27. <https://doi.org/10.18637/jss.v014.i06>
- ZOPPI, U., SKOPEC, Z., SKOPEC, J., JONES, G., FINK, D., HUA, Q., JACOBSEN, G., TUNIZ, C. and WILLIAMS, A. (2004). Forensic applications of  $^{14}\text{C}$  bomb-pulse dating. *Nuclear Instruments and Methods in Physics Research Section B: Beam Interactions with Materials and Atoms* **223** 770–775.